nanomaterials

Article

Investigation of MnO_2 and Ordered Mesoporous Carbon Composites as Electrocatalysts for Li-O_2 Battery Applications

Chih-Chun Chin, Hong-Kai Yang and Jenn-Shing Chen *

Received: 9 November 2015; Accepted: 12 January 2016; Published: 18 January 2016
Academic Editors: Hermenegildo García and Sergio Navalón

Department of Applied Chemistry, National University of Kaohsiung, Kaohsiung City 811, Taiwan; ccchin17@gmail.com (C.-C.C.); hong-kai84@hotmail.com (H.-K.Y.)
* Correspondence: jschen@nuk.edu.tw; Tel.: +886-7-591-9463; Fax: + 886-7-591-9348

Abstract: The electrocatalytic activities of the MnO_2/C composites are examined in Li-O_2 cells as the cathode catalysts. Hierarchically mesoporous carbon-supported manganese oxide (MnO_2/C) composites are prepared using a combination of soft template and hydrothermal methods. The composites are characterized by X-ray powder diffraction, scanning electron microscopy, transmission electron microscopy, small angle X-ray scattering, The Brunauer–Emmett–Teller (BET) measurements, galvanostatic charge-discharge methods, and rotating ring-disk electrode (RRDE) measurements. The electrochemical tests indicate that the MnO_2/C composites have excellent catalytic activity towards oxygen reduction reactions (ORRs) due to the larger surface area of ordered mesoporous carbon and higher catalytic activity of MnO_2. The O_2 solubility, diffusion rates of O_2 and $O_2{}^{\bullet-}$ coefficients (D_{O_2} and $D_{O_2^-}$), the rate constant (k_f) for producing $O_2{}^{\bullet-}$, and the propylene carbonate (PC)-electrolyte decomposition rate constant (k) of the MnO_2/C material were measured by RRDE experiments in the 0.1 M $TBAPF_6/PC$ electrolyte. The values of k_f and k for MnO_2/C are 4.29×10^{-2} cm$\cdot$ s^{-1} and 2.6 s^{-1}, respectively. The results indicate that the MnO_2/C cathode catalyst has higher electrocatalytic activity for the first step of ORR to produce $O_2{}^{\bullet-}$ and achieves a faster PC-electrolyte decomposition rate.

Keywords: MnO_2/C; cathode; lithium-oxygen battery; rotating ring-disk electrode

---

1. Introduction

Energy storage devices with high energy and power densities are being developed for use as power sources for electric vehicles (EV) and hybrid electric vehicles (HEV) [1–3]. Over the past few decades, the vast majority of relevant research has focused on upgrading the performance of conventional lithium-ion batteries for EV or HEV applications; however, their energy densities and specific charge capacities still fail to satisfy commercial requirements such as long-range driving, low cost, and fast charging [1,2,4]. In recent years, rechargeable nonaqueous Li-air batteries have attracted much interest owing to their low cost, environmental friendliness, and high theoretical energy density (~3500 Wh$\cdot$ kg^{-1}), which is nearly equivalent to a nine-fold increase over conventional Li-ion batteries (~400 Wh$\cdot$ kg^{-1}) [4–7]. Despite these favorable characteristics, their practical applications are still hampered by several serious challenges including limited rate capability, poor cycling stability due to the instability of the electrode and electrolyte, and low round-trip efficiency induced by the rather large polarization, resulting in a wide charge–discharge voltage gap [3,8–15]. These critical problems are highly attributable to the O_2 cathode.

A typical rechargeable Li-O_2 battery is constituted by a porous oxygen diffusion cathode, a lithium metal anode, and an Li$^+$-conducting electrolyte. In general, the O_2 cathode is an oxygen catalyst loaded with porous carbon material, which enables both Li_2O_2 deposition (oxygen reduction reactions, ORRs) and decomposition (oxygen evolution reactions, OERs) reactions to occur upon battery discharge and charge, respectively. Many reports [1,4–6,8,9,11,15–18] have pointed out that the electrochemical performance of Li-O_2 batteries depends on many factors such as: the nature and microstructure of the O_2 electrode, electrolyte formula (especially, the composition of solvent), O_2 partial pressure, possible presence of reactive contaminants (e.g., trace water), and the choice of catalysts. In order to enhance the properties of rechargeable Li-O_2 batteries, several strategies have been followed over the years to explore the electrolyte formula, choice, and microstructure design of the O_2 electrode and optimization of the operating parameters [1,3,5,8–11].

Carbon materials with various nanostructures have been developed and used as O_2 cathodes in Li-O_2 batteries [4,6,10,19]. It has been well demonstrated that the performance of Li-O_2 batteries is related to the properties of carbon, such as the morphology, surface area, porous structure, and conductivity [6,9,20]. The design of porous carbon cathodes requires larger intraparticulate voids and open frameworks in their architecture structure to accommodate the insoluble discharge products. These voids and frameworks should help improve discharge capacity and cycling performance [19–21]. Obviously, designing an optimum pore structure for carbon materials can effectively improve the electrochemical performance of Li-O_2 batteries. Although various porous carbon structures have been explored, some studies have demonstrated that hierarchically porous honeycomb-like carbon cathodes with mesoporous/macroporous pore size can increase the specific capacity of Li-O_2 batteries [4–6,15,19–26]. Moreover, it is well known that an ideal cathode catalyst can facilitate the complete reversibility of ORRs and OERs with low polarization in Li-O_2 batteries [21]. Several potential catalysts have recently been proposed to promote ORRs and OERs, including nitrogen-doped carbon, metal oxides, metal nitrides, precious and nonprecious metals, *etc.* [1,3,8,13,15,19,27–29]. Among metal oxides, MnO_2 is a catalyst material of great interest because of its low cost, environmental friendliness, abundance, and electrocatalytic activity for ORRs in Li-O_2 batteries [13,28,30–32]. This study of Li-O_2 batteries focuses on MnO_2-based catalysts.

In the first part of this work, we created a hierarchically mesoporous carbon-supported β-manganese oxide (MnO_2/C) as an O_2 cathode material. We present a detailed study of the Li-O_2 electrochemistry of the MnO_2/C material using an electrolyte of 1 M $LiPF_6$ in a propylene carbonate (PC, which was used in many of the initial works on Li-O_2 batteries) solvent. Although there have been many studies of MnO_2/C materials for Li-O_2 battery applications, few studies have examined the poor stability of the electrolyte due to its reaction with the superoxide radical ($O_2{}^{\bullet -}$) produced upon the discharge at the MnO_2/C electrode. In this work, the stability of the electrolyte against the $O_2{}^{\bullet -}$ of the MnO_2/C electrode was first explored by the RRDE technique. The RRDE was developed about 50 years ago and has been verified to be a powerful tool for the study of electrochemical reactions. RRDE consists of two concentric electrodes (disk and ring electrodes) in a cylindrical holder with both of the electrodes facing downward into the solution. Products generated at the disk reaction are swept outward by the convection caused by rotation, and can be detected electrochemically at the ring by fixing the potential on the ring electrode. In this study, a disk electrode coated with MnO_2/C materials and a Pt ring electrode was fixed at an $O_2{}^{\bullet -}/O_2$ oxidation potential to collect the $O_2{}^{\bullet -}$ ions in electrolytes. Therefore, in the second part, we emphasize aspects of the PC-based electrolyte reaction against $O_2{}^{\bullet -}$ and the related kinetic information of $O_2{}^{\bullet -}$ in the MnO_2/C electrode by studying rotating ring disk electrode (RRDE) experiments and using a lithium-free non-aqueous electrolyte due to the stability of the intermediate $O_2{}^{\bullet -}$. In addition, the oxygen solubility in the electrolyte and the oxygen diffusion velocity throughout the whole O_2 electrode play key roles in determining battery performance, especially at high current densities [33]. In this work, the O_2 solubility, diffusion rates of O_2 and superoxide radical ($O_2{}^{\bullet -}$) coefficients (D_{O_2} and $D_{O_2^-}$), rate constant (k_f) for producing $O_2{}^{\bullet -}$, and PC-electrolyte decomposition rate constant (k) of the MnO_2/C electrode were quantified.

2. Experimental Methods

MnO_2/C composites were prepared by supramolecular self-assembly methods followed by a hydrothermal process. A modification of the mesoporous metal oxides and carbon nanocomposites procedure of Huang *et al.* [34] was applied to synthesize the MnO_2/C composites. The first step was to synthesize a 20 wt. % resol ethanolic solution according to an established method [34,35]. A solution was prepared by dissolving 1.5 g of triblock copolymer Pluronic F127 ($OH(CH_2CH_2O)_n$-$(CH_2CH(CH_3)O)_m$-$(CH_2CH_2O)_nH$, $EO_{106}PO_{70}EO_{106}$, Sigma Aldrich, St. Louis, MO, USA) in 10 g of anhydrous ethanol, then 5 g 20 wt. % resol ethanolic solution and 0.28 g $MnCl_2 \cdot 4H_2O$ (J.T. Baker, 99.8%) were added into the above solution slowly under stirring for 30 min at an ambient temperature. The homogeneous mixture was then transferred into a Petri dish at an ambient temperature for 24 h. After being dried, the films were heated at 100 °C for another 24 h to form orange transparent membranes. The as-made products were scraped from the Petri dish and ground into powders and then calcinated at 400 °C for 5 h under an Ar atmosphere with a heating rate of 1 $^\circ C \cdot min^{-1}$ to yield Mn/C powders. To obtain MnO_2/C composites, the as-prepared Mn/C powders were subjected to a hydrothermal process at 180 °C for 12 h with 0.22 g $KMnO_4$ (J.T. Baker) and 30 mL of deionized water in a Teflon-lined stainless steel autoclave.

A Rigaku-D/MaX-2550 diffractometer (Rigaku, Tokyo, Japan) with Cu K_α radiation (λ = 1.54 Å) was used to obtain X-ray diffraction (XRD) patterns for the samples. Small angle X-ray scattering (SAXS) measurements were taken on a Nanostar U small-angle X-ray scattering system (Bruker, Karlsruhe, Germany) using Cu K_α radiation (40 kV, 35 mA). The morphology of the sample was observed using a scanning electron microscope (SEM, Hitachi S-3400 (Hitachi Limited, Tokyo, Japan)) and transmission electron microscope (TEM, JEOL JEM-3010 (JEOL, Tokyo, Japan)). Selected area electron diffraction (SAED) was applied to examine samples' crystallinity. The Brunauer–Emmett–Teller (BET) method was used to measure the specific surface area of the powders (ASAP2020). The residual carbon content of the samples was measured by an automatic elemental analyzer (EA, Elementar vario, EL III (Elementar Analysensysteme GmbH, Hanau, Germany)).

For electrochemical evaluation, the MnO_2/C electrodes were prepared by wet coating, and were made from as-prepared MnO_2/C composites with super P and a poly(vinylidene difluoride) (PVDF) binder (MKB-212C, Atofina, Serquigny, France) in a weight ratio of 64:16:20. The MnO_2/C composites and super-P were first added to a solution of PVDF in *N*-methyl-2-pyrrolidone (NMP, Riedel-deHaen, Seelze, Germany). To make a slurry with an appropriate viscosity, the mixture was stirred for 20 min at room temperature using a magnetic bar, and then for 5 min using a turbine at 2000 rpm. The resulting slurry was coated onto a piece of separator (Celgard 2400, Charlotte, NC, USA) and dried at 60 °C under vacuum for 12 h. The coating had a thickness of ~100 μm with an active material mass loading of 8 ± 1 $mg \cdot cm^{-2}$. The quantity of active materials on the electrodes was kept constant. Electrodes were dried overnight at 100 °C under a vacuum before being transferred into an argon-filled glove box for cell assembly. The Li-O_2 test cell (EQ-STC-LI-AIR, MTI Corporation, Richmond, CA, USA) was constructed with lithium metal as the negative electrode and the MnO_2/C electrode as the positive electrode. A solution of 1 M $LiPF_6$ in a PC solvent was used as the electrolyte in all cells. After assembly, the test cell was taken away from the Ar-filled glove box and attached to a gas pipe that was constantly purged with dry O_2. Electrochemical tests were carried out after the cell was flushed with O_2 for 6 h. The cells were cycled galvanostatically with a BAT-750B (Acu Tech System, Taipei, Taiwan) at a constant current of 100 mA/g with a voltage region of 2.0–4.3 V *vs.* Li/Li^+ at room temperature.

For the RRDE experiments, the RRDE system (AFMT134DCPTT, Pine Research Instrumention, Durham, NC, USA) with interchangeable disk consisted of a 5 mm diameter glassy carbon electrode and a Pt ring electrode (1 mm width) with a 0.5 mm gap between them. The collection efficiency with this geometry is 0.24. The rotating ring-disk assembly was operated on a Pine AFMSRX rotator and CH705 Bipotentiostat (CH Instruments, Austin, TX, USA) with a computerized interface. Experiments were conducted using a three-electrode cell containing 10 mL of the electrolyte of interest and assembled in a dry Ar-filled AtmosBag (Sigma-Aldrich Z108450, St. Louis, MO, USA). Figure 1 shows the schematic of a four-neck, jacketed glass cell with the RRDE system. The counter electrode was a Li foil connected to a Ni wire, which was isolated by a layer of Celgard 2400 separator to prevent convective oxygen transport to the electrode. The Ag/Ag^+ reference electrode consisted of an Ag wire immersed into 0.1 M $AgNO_3$ in CH_3CN and sealed with a vycor frit at its tip. All potentials in this study were referenced to the Li/Li^+ potential scale (volts *vs.* Li^+/Li or V_{Li+}), obtained by calibration of the reference electrode against a fresh lithium wire before the experiments ($0\ V_{Li} = -3.46 \pm 0.01$ V *vs.* Ag/Ag^+). The working electrode consisted of a catalyst-covered glassy carbon disk and was immersed into the Ar or O_2-purged electrolyte for 30 min before each experiment. Prior to the RRDE measurements, Alternating current (AC) impedance measurements were carried out to determine the uncompensated ohmic electrolyte drop between working and reference electrodes by applying a 10 mV perturbation (0.1 MHz to 10 mHz) at the open circuit. IR (drop) correction to remove ohmic losses was performed by considering a total cell resistance of ~293 Ω measured by AC impedance. The capacitive-corrected ORR currents were calculated by subtracting the current measurement under Ar from that obtained in pure O_2 under identical scan rates, rotation speeds, and catalyst loadings.

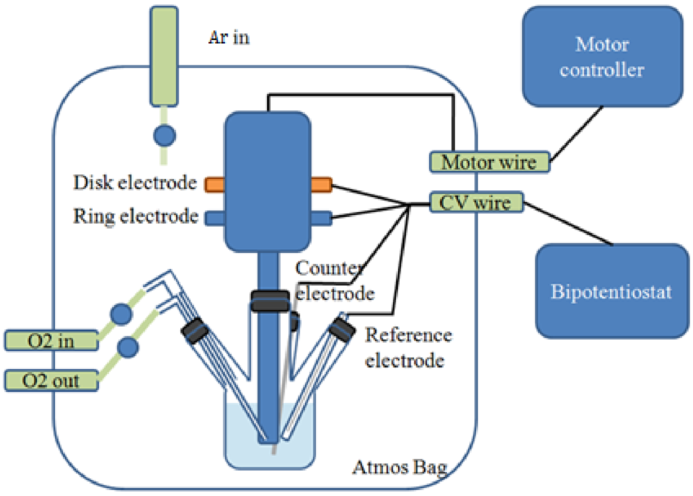

Figure 1. Schematic of a four-neck, jacketed glass cell with a rotating ring-disk electrode (RRDE) system.

3. Results and Discussion

The phase composition and structure of the prepared MnO_2/C composites were examined by the wide-angle XRD and SAXS patterns given in Figure 2a,b. As shown in Figure 2a, all peaks can be identified as a pure and well-crystallized β-MnO_2 phase (JCPDS 24-0735) with an ordered tetragonal structure indexed to the P42/mnm space group. Moreover, the XRD curves did not show any evidence of the formation of crystalline or amorphous carbon. It appears that when using resol/Pluronic F127 templates as a carbon source, the final product is most likely to remain amorphous or in a low crystalline carbon state. The appearance of the scattering peak in the SAXS pattern, as shown in Figure 2b, indicates the long-range regularity and highly ordered nature of the mesoporous structures of the prepared MnO_2/C composite.

The morphology of the prepared MnO_2/C composite was observed using SEM and TEM, as shown in Figure 3a–f. From the SEM images of the MnO_2/C composite (Figure 3a,b), it is clear that the oriented tetragonal MnO_2 nanorods are arranged on the surface of the carbon matrix. The prepared β-MnO_2 nanorods, typically 2–3 μm in length, have a square cross-section with an edge length in the range of 200–300 nm. Figure 3c,d show the TEM images of the MnO_2/C composite at different magnifications. Large domains of highly ordered stripe-like 1D channels are clearly observed. Figure 3e displays a TEM image of a typical nanorod with a smooth surface, and a SAED pattern based on a single nanorod (Figure 3f), indicating single-crystalline nature. The SEM and TEM analysis suggest that hollow MnO_2 nanorods grow homogeneously on the ordered mesoporous carbon frameworks to form the structure of the hierarchically mesoporous MnO_2/C composite.

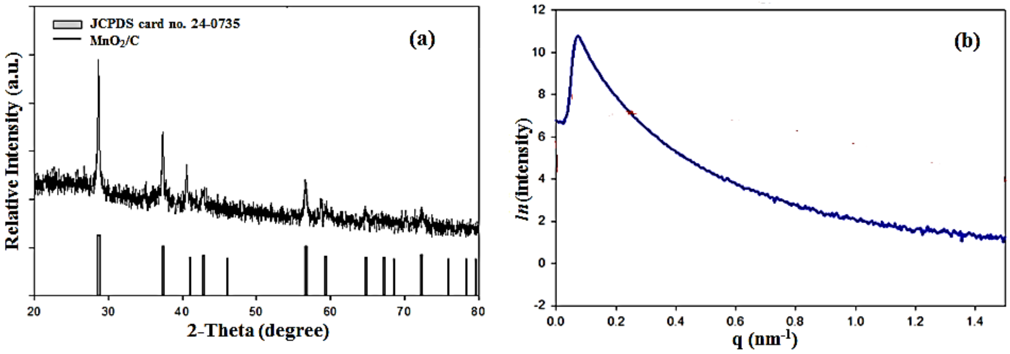

Figure 2. (**a**) Wide-angle X-ray diffraction (XRD) patterns; (**b**) small angle X-ray scattering (SAXS) patterns of MnO_2/C composites.

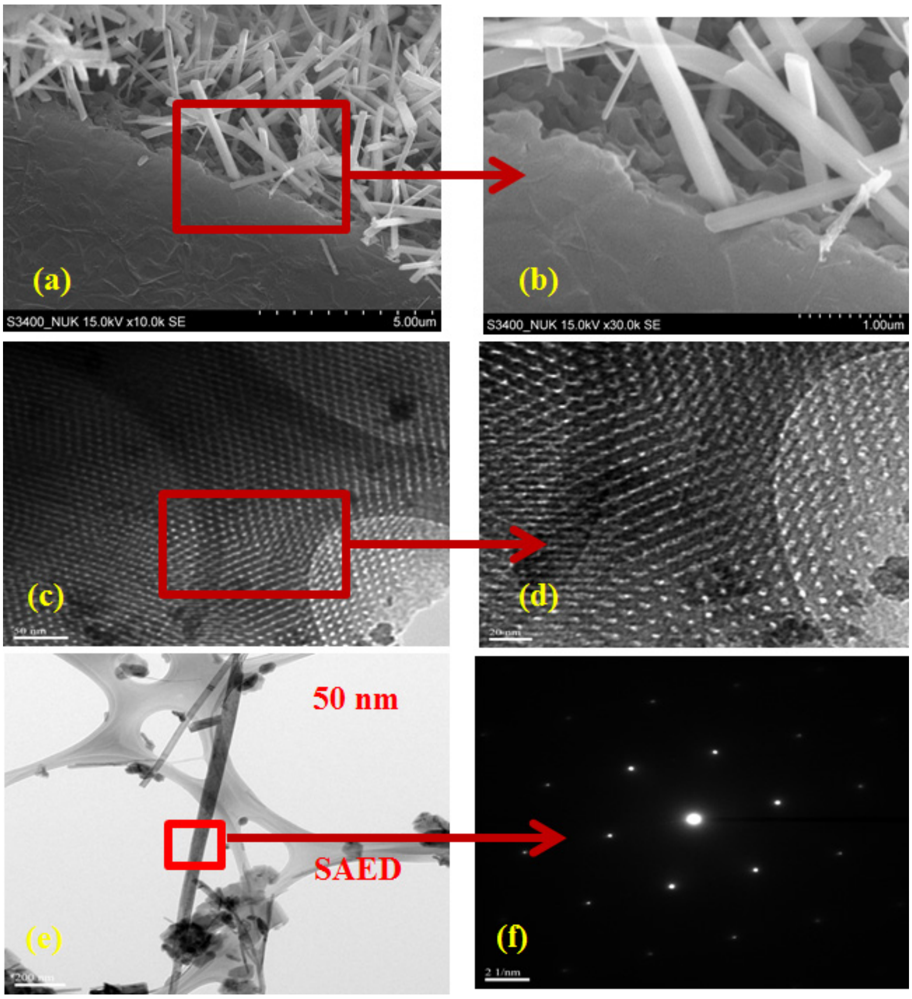

Figure 3. Scanning electron microscope (SEM) images (**a**) MnO_2/C composites; (**b**) high magnification of the region marked with a square in (**a**); and transmission electron microscope (TEM) images (**c**,**e**) MnO_2/C composites; (**d**) high magnification of the region marked with a square in (**c**); and (**f**) selected area electron diffraction (SAED) pattern of the region marked with a square in (**e**).

The pore structure of the mesoporous MnO_2/C composite was determined by nitrogen adsorption-desorption isothermal measurements. As shown in Figure 4, the adsorption isothermal curve of the MnO_2/C composite has a well-defined step as in typical IV classification with a H_1-type hysteretic loop in the p/p_o range of 0.40–1.0, indicating mesoporous material character. These findings suggest that the MnO_2/C composite sample does not contain framework-confined pores but is rather made up of individual nanorods. This is in agreement with the results from the SEM and TEM images. The Barrett–Joyner–Halenda (BJH) pore size distribution for the mesoporous MnO_2/C composite, shown in the insert of Figure 4, reveals peaks centering at 4.8 and 35 nm. This result confirms that most of the pore channels in the ordered mesoporous carbon are not blocked by the loading of MnO_2 nanorods. The nanoarchitecture of ordered mesoporous channels is maintained, which is desirable for the O_2 electrode in Li-O_2 batteries. Moreover, the measured BET surface area of the MnO_2/C composite is relatively high, at about 424 $m^2 \cdot g^{-1}$. The hierarchical microstructure of the MnO_2/C composite results in a large specific surface area. This is important for enhancing the electrochemical properties of an O_2 cathode material.

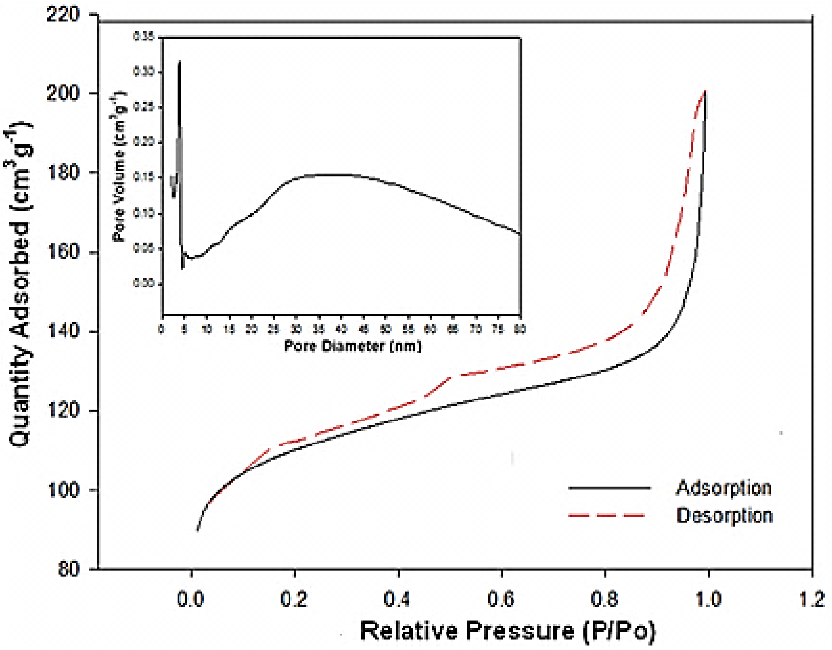

Figure 4. Nitrogen sorption isotherms of MnO_2/C composites. The insert is the Barrett–Joyner–Halenda (BJH) desorption pore size distribution.

MnO_2 has been known as a highly active ORR catalyst for some time [30,32,36] and has recently been applied as an O_2 cathode catalyst in Li-O_2 batteries. Due to the studies of the electrocatalytic activity of MnO_2, the following discussions regarding electrochemical tests make comparisons between Super-P carbon (SP) and MnO_2/C materials. To better study the catalytic activity of the electrodes, cyclic voltammetry (CV) and charge-discharge voltage measurements were carried out. At first, CV was carried out in the Ar-purged electrolyte and subsequently in the same solution saturated with O_2. The capacitively-corrected CV curves derived from both measurements are shown in Figure 5a. The CV plots of the O_2 electrodes prepared from MnO_2/C and SP cycled between 1.5 and 4.5 V with 2 $mV \cdot s^{-1}$ and the O_2-saturated 1 M $LiPF_6/PC$ electrolyte are shown in Figure 5a. From the CV curves, the reduction peak voltage is shifted toward positive voltage, exhibiting electrocatalytic activity in the ORR of both samples. However, the MnO_2/C offers more positive onset reduction peak potential and a larger peak current, which clearly indicate the superior electrocatalytic activity of MnO_2/C compared to SP. Furthermore, the onset oxidation peaks appearing in the CV curves are about 2.7 and 2.9 V for MnO_2/C and SP, respectively. This demonstrates that MnO_2/C, with its lower onset oxidation peak, is more efficient for Li_2O_2 decomposition and has higher catalytic activity for the OER. The initial charge–discharge voltage profiles for both samples are shown in Figure 5b. The charge–discharge profiles of the MnO_2/C electrode exhibit much lower charge overpotential than do those of the SP electrode, although the reduction of the total overpotential is only about 25%. The round-trip efficiencies of the Li-O_2 batteries with a MnO_2/C electrode were lower than those with the SP electrode. These results indicate that the MnO_2/C composite can facilitate the complete reversibility of ORR and OER with low polarization for a Li-O_2 battery. This finding is in good agreement with the CV measurement. The initial discharge capacities of the MnO_2/C and SP electrodes were 612 mAh· g^{-1} and 589 mAh· g^{-1}, respectively. The good electrochemical performance of the MnO_2/C electrode may be due to the hierarchical mesostructure and large specific surface area, and the catalytic activity of the MnO_2/C composite.

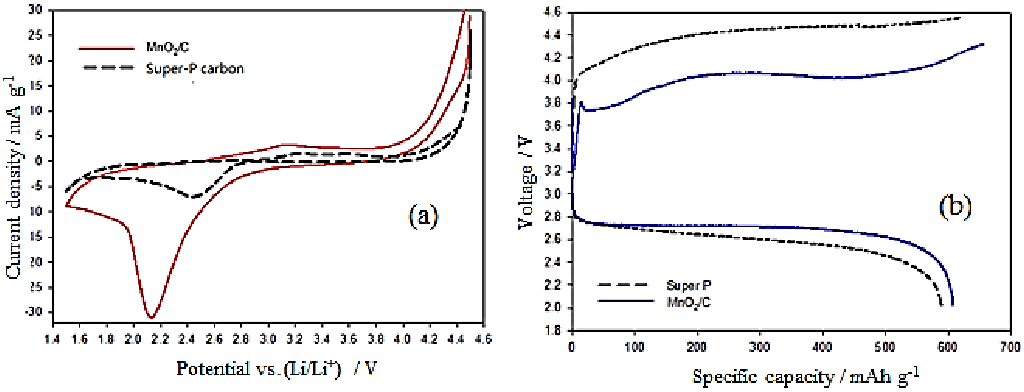

Figure 5. (**a**) CV curves were recorded at a scanning rate of 2 mV· s^{-1} for MnO_2/C and Super-P carbon samples; (**b**) initial charge–discharge profiles for MnO_2/C and Super P samples at a current density of 0.2 mA· cm^{-2}.

The rotating ring disk electrode (RRDE) technique was also used to investigate the kinetics of ORR since the ORR current is strongly relevant to hydrodynamic conditions [31]. Here, we used a glassy carbon (GC) electrode and an as-prepared MnO_2/C composite coated on the GC (MnO_2/C-GC) electrode as the working electrodes to study the stability of the electrolyte at the MnO_2/C electrode. Many reports [1,5,9] have shown the $O_2{}^{\bullet-}$ produced in the first step of the ORR upon battery discharge:

$$O_2 + e^- \xrightarrow{k_f} O_2{}^{\bullet-} \tag{1}$$

The reaction between the $O_2{}^{\bullet-}$ and the electrolyte is the critical problem that causes poor Li-O_2 battery cyclability. In the PC-based electrolyte, the ethereal carbon atom in PC suffers from nucleophilic attacks by $O_2{}^{\bullet-}$, yielding carbonate, acetate, and formate species (among others), according to Equation (2) [37,38]:

$$PC + O_2{}^{\bullet-} \xrightarrow{k} CO_3{}^{2-}, HCOO^-, CH_3COO^- \tag{2}$$

Here, we applied rotating disk electrode (RDE) voltammetry to measure the rate constant (k_f) when reducing O_2 to $O_2{}^{\bullet-}$ for Equation (1) in the 0.1 M $TBAPF_6/PC$ electrolyte. The reaction rate constant, k_f, can be evaluated via the Koutecky–Levich (K–L) equation for a first-order reaction as follows [31]:

$$\frac{1}{i} = \frac{1}{i_k} + \frac{1}{i_d} \tag{3}$$

$$i_k = nFk_fC_{O_2} \tag{4}$$

$$i_d = 0.62nFD_{O_2}{}^{2/3}\nu^{-1/6}C_{O_2}\omega^{1/2} \tag{5}$$

where i_k and i_d represent kinetics and diffusion limiting current density ($\text{A}\cdot\text{m}^{-2}$), respectively; n is the number of electrons exchanged in the electrochemical reaction; F is Faraday's constant (96,485 $\text{C}\cdot\text{mol}^{-1}$); k_f is the rate constant for Equation (1); D_{O_2} is the diffusion coefficient of O_2 in the solution; ν is the kinematic viscosity; ω is the angular frequency of the rotation; and C_{O_2} is the saturation concentration of O_2 in the solution. Additionally, knowing the values of ν and D_{O_2} for an electrolyte, one can obtain the concentration of oxygen (C_{O_2}) and rate constant (k_f) for Equation (1) by linearly fitting the K-L plots of i^{-1} *vs.* $\omega^{-0.5}$, as follows

$$\frac{1}{i} = \frac{1}{i_k} + \frac{1}{0.62nFD_{O_2}^{2/3}\nu^{-1/6}C_{O_2}\omega^{1/2}} \tag{6}$$

Prior to estimating the value of k_f from the K–L equation, the kinematic viscosity (ν) of the electrolyte and the diffusion coefficients of O_2 and $O_2^{\bullet-}$ (D_{O_2} and $D_{O_2^-}$), need to be quantified. The value of ν for PC with 0.1 M TBAPF_6 is 2.59×10^{-2} $\text{cm}^2\cdot\text{s}^{-1}$ at 25 °C (ρ = 1.2 $\text{g}\cdot\text{mL}^{-1}$ and η = 3.13 mPa·s) and was measured by a Rheometer (Malvern Gemini, Malvern Instruments Ltd., Malvern, UK). For a known viscosity, the diffusion coefficients can be directly determined from the transit-time (T_s) measurement by the RRDE technique, as reported previously [37,39]. Figure 6a shows an example of T_s measurement in O_2-saturated solutions of 0.1 M TBAPF_6 in PC at ω = 100 rpm; T_s, the origin of which is taken at time = 2 s (the time at which the disk is conducted cathodic potential at 1.85 V_{Li}), is measured graphically from the intercept of the base steady ring current and the fast attenuate ring current line. Figure 6b,c show measurements of steady ring currents at the rotation rates (ω) of different electrodes, yielding T_s values for O_2 and $O_2^{\bullet-}$. Then, the obtained T_s is related to the ω and the ratio of ν and the diffusion coefficient (D), according to Equation (7) [37,39]:

$$T_s = \text{K}\left(\frac{\nu}{D}\right)^{1/3}\omega^{-1} \tag{7}$$

where K is proportionally constant depending on the RRDE's geometry; $\text{K} = 43.1[\log(r_2/r_1)]^{2/3}$ (for T_s, reported in s and ω in rpm). For the RRDE used here, with r_1 = 0.25 cm and r_2 = 0.325 cm, the value of K is 10.1 rpm·s. Table 1 shows the estimated values of the diffusion coefficients of O_2 and $O_2^{\bullet-}$ calculated from Equation (7) based on the slopes of T_s *vs.* ω^{-1} obtained from Figure 6d. Figure 7a shows that well-defined O_2 diffusion-limited currents are obtained for the ORR on a GC electrode in an O_2-saturated 0.1 M TBAPF_6/PC solution. The K–L plot for the disk current values at 1.50 V_{Li} reveals the expected linear relation between the inverse of the limiting current and $\omega^{-0.5}$ (see Equation (6)). As shown in Table 1, the concentration of oxygen (C_{O_2}) on the GC electrode was estimated from the slope of the K–L plot using the prior measured values of ν and D_{O_2}, where n = 1 (according to the reaction of Equation (1)). The value of C_{O_2} is 6.1 M, which is higher than the finding of a previous report (4.8 M) [37]. This can be attributed to the larger O_2 flow rate in this experiment. The estimated value of C_{O_2} was also applied in the following calculations of the MnO_2/C-GC electrode since the same operation parameters (*i.e.*, O_2 flow rate, electrolyte composition, and amount) were used, as listed in Table 1. The rate constant for producing $O_2^{\bullet-}$, k_f for GC and the MnO_2/C-GC electrodes can be obtained by linearly fitting the K–L plots of i^{-1} *vs.* $\omega^{-0.5}$ (see Equation (6)), as shown in Figure 7a,b. The values of k_f for GC and the MnO_2/C-GC electrodes are 1.92×10^{-2} $\text{cm}\cdot\text{s}^{-1}$ and 4.29×10^{-2} $\text{cm}\cdot\text{s}^{-1}$, respectively. This result indicates that the MnO_2/C cathode catalyst exhibits a larger k_f value, resulting from higher electrocatalytic activity for the first step of the ORR (see Equation (1)) which produces a higher concentration of $O_2^{\bullet-}$.

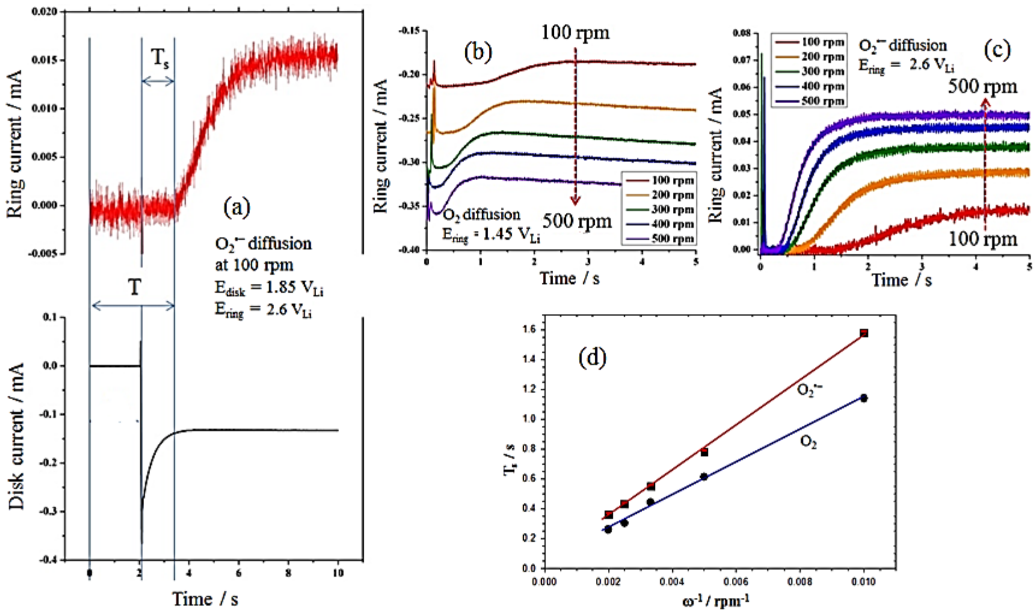

Figure 6. (**a**) Example of determination of the superoxide radical ($O_2^{•-}$) transit-time (T_s) in O_2-saturated solutions of 0.1 M $TBAPF_6$ in propylene carbonate (PC) at ω = 100 rpm, E_{disk} = 1.85 V and E_{ring} = 2.6 V. Transit time (*Ts*) values at different rotation rates for the diffusion of (**b**) O_2 and (**c**) $O_2^{•-}$; (**d**) relation between the inverse of the rotation speed and the transient time for O_2 and $O_2^{•-}$.

Table 1. Summary of the electrolyte properties estimated with the proposed RRDE-based methodology and comparison with findings reported in the literature.

Disk Material/Electrolyte	ν ($cm^2 \cdot s^{-1}$)	D_{O_2} ($cm^2 \cdot s^{-1}$)	$D_{O_2^-}$ ($cm^2 \cdot s^{-1}$)	C_{O_2} (mM)	Reference
GC/0.1 M $TBAPF_6$, PC	2.6×10^{-2}	1.9×10^{-5}	8.6×10^{-6}	6.1	This work
MnO_2/C-GC/0.1 M $TBAPF_6$, PC	2.6×10^{-2}	1.9×10^{-5}	1.8×10^{-6}	6.1	This work
GC/0.2M TBATFSI, PC	2.6×10^{-2}	2.5×10^{-5}	6.8×10^{-6}	4.8	[37]

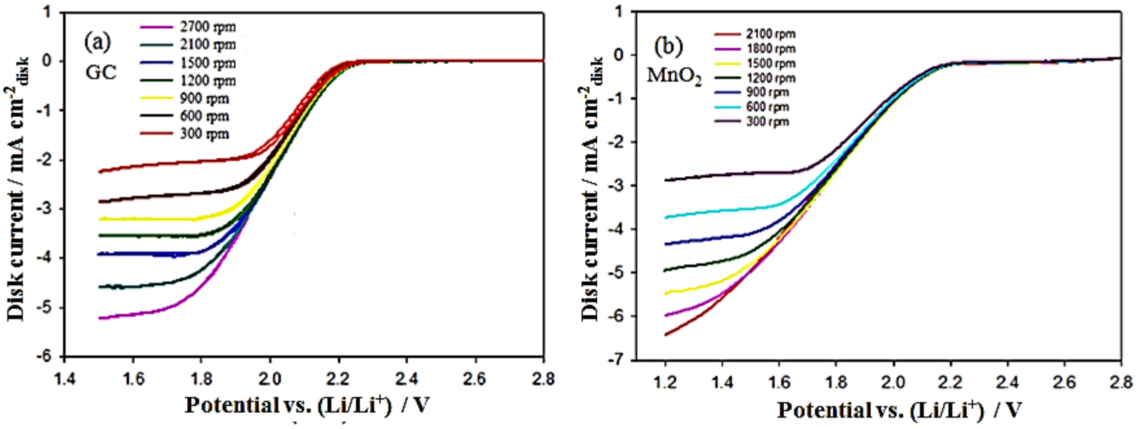

Figure 7. (**a**) Steady-state CV curves of a glassy carbon rotating disk electrode (RDE) in an O_2-saturated 0.1 M $TBAPF_6$/PC solution at a scan rate of 50 mV/s between 1.5 and 2.8 V_{Li} with different rotation rates. The insert is the Koutecky–Levich plot derived from the disc current values at 1.50 V_{Li}; (**b**) steady-state CV curves of a MnO_2/C RDE in an O_2-saturated 0.1 M $TBAPF_6$/PC solution at a scan rate of 50 mV/s between 1.2 and 2.8 V_{Li} with different rotation rates.

Recently, Herranz *et al.* [37] used RRDE voltammetry to quantify the stability of an electrolyte against $O_2^{\bullet -}$ by the rate constant (k) for Equation (2) According to their methods, the $O_2^{\bullet -}$ produced at the disk electrode in Equation (1) and the amount of $O_2^{\bullet -}$ were quantified at the ring electrode. The amount of $O_2^{\bullet -}$ consumed depends on the effective transient time, T_s, between the disk and the ring and the rate constant, k, for Equation (2). Longer T_s and larger k values cause increasing consumption of $O_2^{\bullet -}$ due to its reaction with the electrolyte, resulting in a lower $O_2^{\bullet -}$ oxidation current at the ring. Therefore, the collection efficiency, N_k, for $O_2^{\bullet -}$ at the ring electrode decreases with increasing transient time, which, in turn, depends on the geometry of ring and disk electrode, the diffusion coefficient of $O_2^{\bullet -}$ in the electrolyte, $D_{O_2^-}$, and the electrode rotation speed, ω. The correlation with the collection efficiency is the absolute ratio of ring and disk currents and can be characterized by the following equation [37,40]:

$$N_k = -\frac{i_{ring}}{i_{disk}} = N_{geometrical} - \beta^{\frac{2}{3}}\left(1 - UA_1^{-1}\right) + \frac{1}{2}A_1^{-1}A_2^2\kappa^2 U\beta^{\frac{4}{3}} - 2A_2\kappa^2 T_2 \tag{8}$$

where $A_1 = 1.288$, $A_2 = 0.643\ \nu^{1/6}\ D_{O_2^-}{}^{1/3}$, $\beta = 3\ln(r_3/r_2)$, $U = k^{-1}\tanh(A_1 k)$ and $T_2 = 0.718\ln(r_2/r_1)$, whereby r_1–r_3 refer to the radius of the disk and internal and external ring radii, respectively; ν is the kinematic viscosity; ω is the rotation rate; k is the rate constant for Equation (2); and $D_{O_2^-}$ is the diffusion coefficient of $O_2^{\bullet -}$. $N_{geometrical}$ is the geometrical collection efficiency of the RRDE corresponding to the fraction of a species electrochemically generated at the disk. This species is detected at the ring due to the lack of side-reactions with the electrolyte. Equation (8) shows the variation of N_k where the rotation rate and the rate constant (k) can be calculated at higher rotation rates, which show that the N_k is close to a constant value. Figure 8a shows the RRDE profiles of the MnO_2/C sample coating on the disk electrode. The disk and ring currents are recorded in an O_2-saturated 0.1 M $TBAPF_6/PC$ solution at rotation rates between 300 and 2100 rpm, with continuous holding of the Pt ring at 2.85 V_{Li}. The ring current increases with the rotation rates because the shorter transient time at higher rotation rates reduces the reaction time between $O_2^{\bullet -}$ and the PC electrolyte so that a higher concentration of superoxide radical can be oxidized at the ring. Also, the N_k increases with rotation rates (ω) and is close to a constant value (0.14) at ω = 2100 rpm, as shown in Figure 8b. The PC-electrolyte decomposition rate constant (k) can be calculated by Equation (8) using the N_k value at a rotation speed of 2100 rpm with the kinematic viscosity (ν) and $D_{O_2^-}$ listed in Table 1. Table 2 shows the rate constant for producing $O_2^{\bullet -}$, k_f, and the PC-electrolyte decomposition rate constant, k, on the GC and MnO_2/C-GC electrodes. The value of k (1.5 s^{-1}) on the GC electrode is close to that of a previously reported measurement (k = 1.3 s^{-1}) [37]. Obviously, the k value on the MnO_2/C-GC electrode of 2.6 s^{-1} is larger than that on the GC electrode. This result shows that MnO_2/C is more active for the first step of the ORR (larger rate constant; k_f), producing a higher concentration of $O_2^{\bullet -}$ and leading to faster PC-electrolyte decomposition due to the attack by a large amount of $O_2^{\bullet -}$. Therefore, it is important to choose an appropriate electrolyte to avoid decomposition by $O_2^{\bullet -}$ attack for highly active catalyst applications on the cathode materials in Li-O_2 batteries. More detailed RRDE experiments and analysis will be carried out to estimate the decomposition rates of various electrolytes with different active catalysts.

Table 2. The rate constant for producing $O_2^{\bullet -}$, k_f, and the PC-electrolyte decomposition rate constant, k, on the GC and MnO_2/C-GC electrodes.

Disk Material/Electrolyte	k_f ($cm \cdot s^{-1}$)	k (s^{-1})	Reference
GC/0.1 M $TBAPF_6$, PC	1.9×10^{-2}	1.5	This work
MnO_2/C-GC/0.1 M $TBAPF_6$, PC	4.3×10^{-2}	2.6	This work
GC/0.2M TBATFSI, PC		1.3	[37]

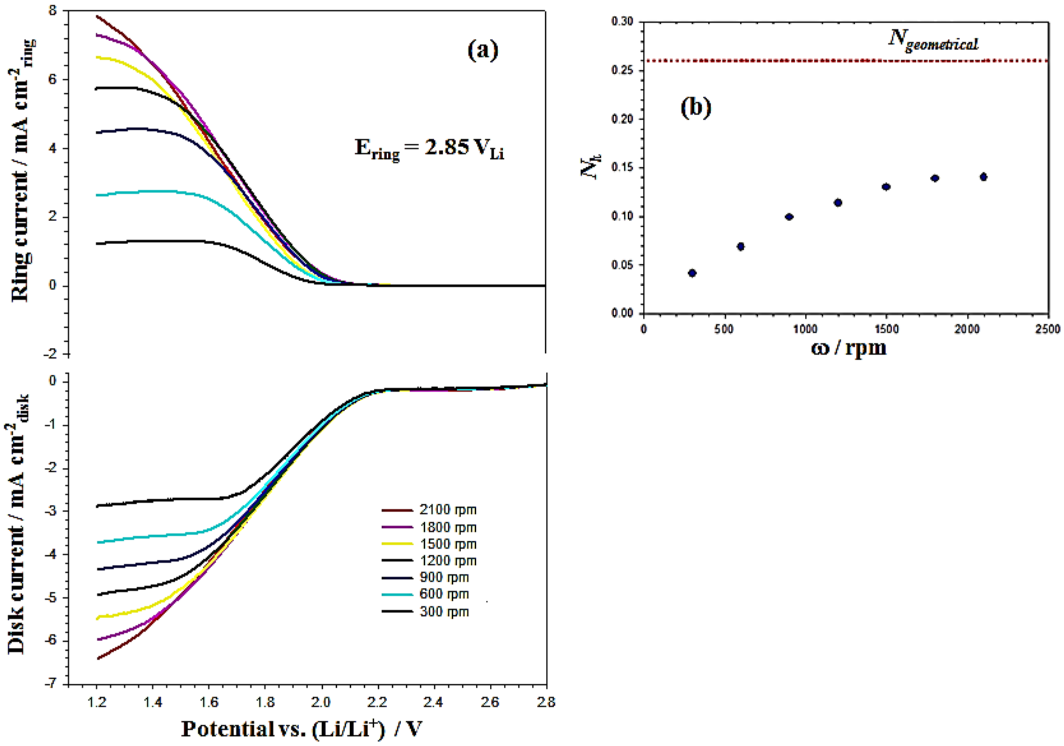

Figure 8. (**a**) RRDE profiles of MnO_2/C recorded at 50 $mV\cdot s^{-1}$ in an O_2-saturated 0.1 M $TBAPF_6/PC$ solution, at rotation rates between 300 and 2100 rpm with continuous holding of the Pt ring at 2.85 V_{Li}; (**b**) evolution of the absolute ratio between the ring and disk current (N_k) and the electrode rotation speed (ω).

4. Conclusions

A hierarchically mesoporous carbon-supported manganese oxide (MnO_2/C) has been synthesized by a combination of soft template and hydrothermal methods. SEM and TEM analysis confirmed that hollow MnO_2 nanorods grow homogeneously on ordered mesoporous carbon frameworks to form a hierarchically mesoporous MnO_2/C composite structure. The CV and galvanostatic charge–discharge tests indicate that MnO_2/C composites have excellent catalytic activity towards ORR due to the larger surface area of ordered mesoporous carbon and higher catalytic activity of MnO_2.

The O_2 solubility, the diffusion rates of O_2 and $O_2^{\bullet-}$ coefficients, the rate constant for producing $O_2^{\bullet-}$ (k_f), and the PC-electrolyte decomposition rate constant (k) of the MnO_2/C composites have been measured by RRDE experiments and analysis in the 0.1 M $TBAPF_6/PC$ electrolyte. The results indicate that MnO_2/C is more active for the first step of the ORR (larger rate constant; k_f), produces a higher concentration of $O_2^{\bullet-}$, and leads to faster PC-electrolyte decomposition due to the attack by a large amount of $O_2^{\bullet-}$. The stability of the electrolyte is very important when applying an active catalyst on a cathode material in Li-O_2 batteries. More detailed RRDE experiments and analysis will be carried out to estimate the decomposition rates of various electrolytes. These results seem to be interesting for the design of advanced Li-O_2 batteries with high electrochemical performance.

Acknowledgments: The authors thank the Ministry of Science and Technology of Taiwan for the financial support for this work under contract No. NSC-102-2113-M-390-005-MY3.

Author Contributions: Chih-Chun Chin and Hong-Kai Yang performed the experiments and analyzed the data. Jenn-Shing Chen contributed to the idea, discussion and writing the manuscript.

Conflicts of Interest: The authors declare no conflict of interest.

References

1. Bhatt, M.D.; Geaney, H.; Nolan, M.; O'Dwyer, C. Key scientific challenges in current rechargeable non-aqueous Li-O_2 batteries: Experiment and theory. *Phys. Chem. Chem. Phys.* **2014**, *16*, 12093–12130. [CrossRef] [PubMed]
2. Rezvanizaniani, S.M.; Liu, Z.; Chen, Y.; Lee, J. Review and recent advances in battery health monitoring and prognostics technologies for electric vehicle (EV) safety and mobility. *J. Power Sources* **2014**, *256*, 110–124. [CrossRef]
3. Lu, J.; Li, L.; Park, J.B.; Sun, Y.K.; Wu, F.; Amine, K. Aprotic and aqueous Li-O_2 batteries. *Chem. Rev.* **2014**, *114*, 5611–5640. [CrossRef] [PubMed]
4. Etacheri, V.; Sharon, D.; Garsuch, A.; Afri, M.; Frimer, A.A.; Aurbach, D. Hierarchical activated carbon microfiber (ACM) electrodes for rechargeable Li-O_2 batteries. *J. Mater. Chem. A* **2013**, *1*, 5021–5030. [CrossRef]
5. Capsoni, D.; Bini, M.; Ferrari, S.; Quartarone, E.; Mustarelli, P. Recent advances in the development of Li-air batteries. *J. Power Sources* **2012**, *220*, 253–263. [CrossRef]
6. Ding, N.; Chien, S.W.; Hor, T.S.A.; Lum, R.; Zong, Y.; Liu, Z. Influence of carbon pore size on the discharge capacity of Li-O_2 batteries. *J. Mater. Chem. A* **2014**, *2*, 12433–12441. [CrossRef]
7. Bruce, P.G.; Freunberger, S.A.; Hardwick, L.J.; Tarascon, J.M. Li-O_2 and Li-S batteries with high energy storage. *Nat. Mater.* **2012**, *11*, 19–29. [CrossRef] [PubMed]
8. Yoon, T.H.; Park, Y.J. New strategy toward enhanced air electrode for Li-air batteries: apply a polydopamine coating and dissolved catalyst. *RSC Adv.* **2014**, *4*, 17434–17442. [CrossRef]
9. Xu, L.; Ma, J.; Li, B.; Kang, F. A novel air electrode design: A key to high rate capability and long life span. *J. Power Sources* **2014**, *255*, 187–196. [CrossRef]
10. Wang, J.; Li, Y.; Sun, X. Challenges and opportunities of nanostructured materials for aprotic rechargeable lithium-air batteries. *Nano Energy* **2013**, *2*, 443–467. [CrossRef]
11. Padbury, R.; Zhang, X. Lithium-oxygen batteries-limiting factors that affect performance. *J. Power Sources* **2011**, *196*, 4436–4444. [CrossRef]
12. Lu, Y.C.; Gasteiger, H.A.; Shao-Horn, Y. Catalytic activity trends of oxygen reduction reaction for nonaqueous Li-air batteries. *J. Am. Chem. Soc.* **2011**, *133*, 19048–19051. [CrossRef] [PubMed]
13. Park, H.W.; Lee, D.U.; Nazar, L.F.; Chen, Z. Oxygen reduction reaction using MnO_2 nanotubes/nitrogen-doped exfoliated graphene hybrid catalyst for Li-O_2 battery applications. *J. Electrochem. Soc.* **2013**, *160*, A344–A350. [CrossRef]
14. Zhang, Z.; Zhou, G.; Chen, W.; Lai, Y.; Li, J. Facile synthesis of Fe_2O_3 nanoflakes and their electrochemical properties for Li-air batteries. *ECS Electrochem. Lett.* **2014**, *3*, A8–A10. [CrossRef]
15. Li, J.; Zhao, Y.; Zou, M.; Wu, C.; Huang, Z.; Guan, L. An Effective Integrated Design for Enhanced Cathodes of Ni Foam-Supported Pt/Carbon Nanotubes for Li-O_2 Batteries. *ACS Appl. Mater. Interfaces* **2014**, *6*, 12479–12485. [CrossRef] [PubMed]
16. McCloskey, B.D.; Scheffler, R.; Spidel, A.; Girishkumar, G.; Luntz, A.C. On the mechanism of nonaqueous Li-O_2 electrochemistry on C and its kinetic overpotentials: some implications for Li-air batteries. *J. Phys. Chem. C* **2012**, *116*, 23897–23905. [CrossRef]
17. Meini, S.; Solchenbach, S.; Piana, M.; Gasteiger, H.A. The role of electrolyte solvent stability and electrolyte impurities in the electrooxidation of Li_2O_2 in Li-O_2 batteries. *J. Electrochem. Soc.* **2014**, *161*, A1306–A1314. [CrossRef]
18. Lu, Y.-C.; Gasteiger, H.A.; Shao-Horn, Y. Method development to evaluate the oxygen reduction activity of high-surface-area catalysts for Li-air batteries. *Electrochem. Solid-State Lett.* **2011**, *14*, A70–A74. [CrossRef]
19. Sun, B.; Huang, X.; Chen, S.; Munroe, P.; Wang, G. Porous graphene nanoarchitectures: An efficient catalyst for low charge-overpotential, long life, and high capacity lithium-oxygen batteries. *Nano Lett.* **2014**, *14*, 3145–3152. [CrossRef] [PubMed]
20. Chervin, C.N.; Wattendorf, M.J.; Long, J.W.; Kucko, N.W.; Rolison, D.R. Carbon nanofoam-based cathodes for Li-O_2 batteries: Correlation of pore-solid architecture and electrochemical performance. *J. Electrochem. Soc.* **2013**, *160*, A1510–A1516. [CrossRef]
21. Lu, F.; Cao, X.; Wang, Y.; Jin, C.; Shen, M.; Yang, R. A hierarchical $NiCo_2O_4$ spinel nanowire array as an electrocatalyst for rechargeable Li-air batteries. *RSC Adv.* **2014**, *4*, 40373–40376. [CrossRef]

22. Xiao, J.; Mei, D.; Li, X.; Xu, W.; Wang, D.; Graff, G.L.; Bennett, W.D.; Nie, Z.; Saraf, L.V.; Aksay, I.A.; *et al*. Hierarchically porous graphene as a lithium-air battery electrode. *Nano Lett.* **2011**, *11*, 5071–5078. [CrossRef] [PubMed]
23. Cao, R.; Thapa, R.; Kim, H.; Xu, X.; Kim, M.G.; Li, Q.; Park, N.; Liu, M.; Cho, J. Promotion of oxygen reduction by a bio-inspired tethered iron phthalocyanine carbon nanotube-based catalyst. *Nature Commun.* **2013**, *4*, 2076–2082. [CrossRef] [PubMed]
24. Guo, Z.; Zhou, D.; Dong, X.; Qiu, Z.; Wang, Y.; Xia, Y. Ordered hierarchical mesoporous/macroporous carbon: A high-performance catalyst for rechargeable Li-O_2 batteries. *Adv. Mater.* **2013**, *25*, 5668–5672. [CrossRef] [PubMed]
25. Sun, B.; Liu, H.; Munroe, P.; Ahn, H.; Wang, G. Nanocomposites of CoO and a mesoporous carbon (CMK-3) as a high performance cathode catalyst for lithium-oxygen batteries. *Nano Res.* **2012**, *5*, 460–469. [CrossRef]
26. Wang, Z.-L.; Xu, D.; Xu, J.-J.; Zhang, L.-L.; Zhang, X.-B. Graphene oxide gel-derived, free-standing, hierarchically porous carbon for high-capacity and high-rate rechargeable Li-O_2 batteries. *Adv. Funct. Mater.* **2012**, *22*, 3699–3705. [CrossRef]
27. Li, Y.; Wang, J.; Li, X.; Geng, D.; Banis, M.N.; Li, R.; Sun, X. Nitrogen-doped graphene nanosheets as cathode materials with excellent electrocatalytic activity for high capacity lithium-oxygen batteries. *Electrochem. Commun.* **2012**, *18*, 12–15. [CrossRef]
28. Cheng, H.; Scott, K. Carbon-supported manganese oxide nanocatalysts for rechargeable lithium–air batteries. *J. Power Sources* **2010**, *195*, 1370–1374. [CrossRef]
29. Park, H.W.; Lee, D.U.; Liu, Y.; Wu, J.; Nazar, L.F.; Chen, Z. Bi-functional N-doped CNT/graphene composite as highly active and durable electrocatalyst for metal air battery applications. *J. Electrochem. Soc.* **2013**, *160*, A2244–A2250. [CrossRef]
30. Yu, Y.; Zhang, B.; Xu, Z.-L.; He, Y.-B.; Kim, J.-K. Free-standing Ni mesh with *in-situ* grown MnO_2 nanoparticles as cathode for Li-air batteries. *Solid State Ionics* **2014**, *262*, 197–201. [CrossRef]
31. Xiao, W.; Wang, D.; Lou, X.W. Shape-controlled synthesis of MnO_2 nanostructures with enhanced electrocatalytic activity for oxygen reduction. *J. Phys. Chem. C* **2010**, *114*, 1694–1700. [CrossRef]
32. Debart, A.; Paterson, A.J.; Bao, J.; Bruce, P.G. α-MnO_2 nanowires: A catalyst for the O_2 electrode in rechargeable lithium batteries. *Angew. Chem.* **2008**, *47*, 4521–4524. [CrossRef] [PubMed]
33. Landa-Medrano, I.; Pinedo, R.; de Larramendi, I.R.; Ortiz-Vitoriano, N.; Rojo, T. Monitoring the location of cathode-reactions in Li-O_2 batteries. *J. Electrochem. Soc.* **2015**, *162*, A3126–A3132. [CrossRef]
34. Huang, C.-H.; Gu, D.; Zhao, D.; Doong, R.-A. Direct synthesis of controllable microstructures of thermally stable and ordered mesoporous crystalline titanium oxides and carbide/carbon composites. *Chem. Mater.* **2010**, *22*, 1760–1767. [CrossRef]
35. Meng, Y.; Gu, D.; Zhang, F.; Shi, Y.; Yang, H.; Li, Z.; Yu, C.; Tu, B.; Zhao, D. Ordered mesoporous polymers and homologous carbon frameworks: Amphiphilic surfactant templating and direct transformation. *Angew. Chem.* **2005**, *44*, 7053–7059. [CrossRef] [PubMed]
36. Wang, Z.-L.; Xu, D.; Xu, J.-J.; Zhang, X.-B. Oxygen electrocatalysts in metal-air batteries: From aqueous to nonaqueous electrolytes. *Chem. Soc. Rev.* **2014**, *43*, 7746–7786. [CrossRef] [PubMed]
37. Herranz, J.; Garsuch, A.; Gasteiger, H.A. Using rotating ring disc electrode voltammetry to quantify the superoxide radical stability of aprotic Li-air battery electrolytes. *J. Phys. Chem. C* **2012**, *116*, 19084–19094. [CrossRef]
38. Freunberger, S.A.; Chen, Y.; Peng, Z.; Griffin, J.M.; Hardwick, L.J.; Barde, F.; Novak, P.; Bruce, P.G. Reactions in the rechargeable lithium-O_2 battery with alkyl carbonate electrolytes. *J. Am. Chem. Soc.* **2011**, *133*, 8040–8047. [CrossRef] [PubMed]
39. Chatenet, M.; Molina-Concha, M.B.; El-Kissi, N.; Parrour, G.; Diard, J.P. Direct rotating ring-disk measurement of the sodium borohydride diffusion coefficient in sodium hydroxide solutions. *Electrochim. Acta* **2009**, *54*, 4426–4435. [CrossRef]
40. Bard, A.J.; Faulkner, L.R. *Electrochemical Methods: Fundamentals and Applications*; John Wiely & Sons: New York, NY, USA, 2001; p. 519.

© 2016 by the authors; licensee MDPI, Basel, Switzerland. This article is an open access article distributed under the terms and conditions of the Creative Commons by Attribution (CC-BY) license (http://creativecommons.org/licenses/by/4.0/).